Earth and Planetary Science Letters 401 (2014) 1–11

Contents lists available at ScienceDirect

Earth and Planetary Science Letters

www.elsevier.com/locate/epsl

Distribution of dissolved water in magmatic glass records growth and resorption of bubbles

I.M. McIntosh [a,c,*], E.W. Llewellin [a], M.C.S. Humphreys [a,b], A.R.L. Nichols [c], A. Burgisser [d,e], C.I. Schipper [d,e,f], J.F. Larsen [g]

[a] Department of Earth Sciences, Durham University, Science Labs, Durham, DH1 3LE, UK [1]
[b] Department of Earth Sciences, University of Oxford, South Parks Road, Oxford, OX1 3AN, UK
[c] Research and Development Center for Ocean Drilling Science, Japan Agency for Marine Earth Science and Technology (JAMSTEC), 2-15 Natsushima-cho, Yokosuka, Kanagawa 237-0061, Japan
[d] Institut des Sciences de la Terre, CNRS – IRD – Université de Savoie, Campus Scientifique, 73376 Le Bourget du Lac, France
[e] Institut des Sciences de la Terre (ISTO), Centre National de la Recherche Scientifique (CNRS), l'Université d'Orléans, 1a rue de la Férollerie, Orléans Cedex 2, 45071, France [2]
[f] School of Geography, Environment and Earth Sciences, Victoria University of Wellington, PO Box 600, Wellington 6140, New Zealand [3]
[g] Geophysical Institute, University of Alaska, Fairbanks, AK 99775, United States

ARTICLE INFO

Article history:
Received 15 September 2013
Received in revised form 12 May 2014
Accepted 21 May 2014
Available online xxxx
Editor: T. Elliott

Keywords:
bubble growth
bubble resorption
diffusion
quench effect
water speciation
disequilibrium

ABSTRACT

Volcanic eruptions are driven by the growth of gas bubbles in magma. Bubbles grow when dissolved volatile species, principally water, diffuse through the silicate melt and exsolve at the bubble wall. On rapid cooling, the melt quenches to glass, preserving the spatial distribution of water concentration around the bubbles (now vesicles), offering a window into pre-eruptive conditions. We measure the water distribution around vesicles in experimentally-vesiculated samples, with high spatial resolution. We find that, contrary to expectation, water concentration increases towards vesicles, indicating that water is resorbed from bubbles during cooling; textural evidence suggests that resorption occurs largely before the melt solidifies. Speciation data indicate that the molecular water distribution records resorption, whilst the hydroxyl distribution records earlier decompressive growth. Our results challenge the emerging paradigm that resorption indicates fluctuating pressure conditions, and lay the foundations for a new tool for reconstructing the eruptive history of natural volcanic products.

1. Introduction

Bubbles nucleate when magmatic volatiles (species such as water, CO_2 and SO_2, that are only weakly soluble in the silicate melt) exsolve from a supersaturated melt. Water is the most important volatile because it is usually the most abundant and because it strongly affects melt viscosity (Hess and Dingwell, 1996). It is dissolved in the melt as two principal species: molecular water, H_2O_m, and hydroxyl groups, OH. As magma ascends, bubbles grow through decompressive expansion and continuing exsolution of volatiles from the melt (Sparks, 1978). Together these processes control the bubble growth rate which, in turn, controls or influences almost every aspect of magma ascent and eruption, including: magma vesicularity, buoyancy, rheology and permeability; the pressure gradient that drives the eruption; and the onset of magma fragmentation. Understanding and quantifying bubble growth is, therefore, one of the most fundamental challenges in physical volcanology.

Water exsolves from the melt, into a bubble, when its solubility in the melt decreases, and resorbs into the melt when its solubility increases. The resulting change in the water concentration at the bubble wall creates a chemical potential gradient in the melt, which drives diffusion towards a growing bubble and away from a shrinking bubble (Fig. 1). The water concentration profile may be preserved when the melt quenches to glass, offering the tantalising prospect of reconstructing the bubble's history of growth and resorption. We quantify the spatial distribution of dissolved water and its species in experimentally-vesiculated magmatic glasses, using secondary ion mass spectrometry (SIMS)-calibrated backscatter

* Corresponding author at: Research and Development Center for Ocean Drilling Science, Japan Agency for Marine Earth Science and Technology (JAMSTEC), 2-15 Natsushima-cho, Yokosuka, Kanagawa 237-0061, Japan. Tel.: +81 46867 9766; fax: +81 46867 9625.
E-mail address: i.m.mcintosh@jamstec.go.jp (I.M. McIntosh).
[1] Current address of the author M.C.S. Humphreys.
[2] Current address of the author A. Burgisser.
[3] Current address of the author C.I. Schipper.

http://dx.doi.org/10.1016/j.epsl.2014.05.037
0012-821X/

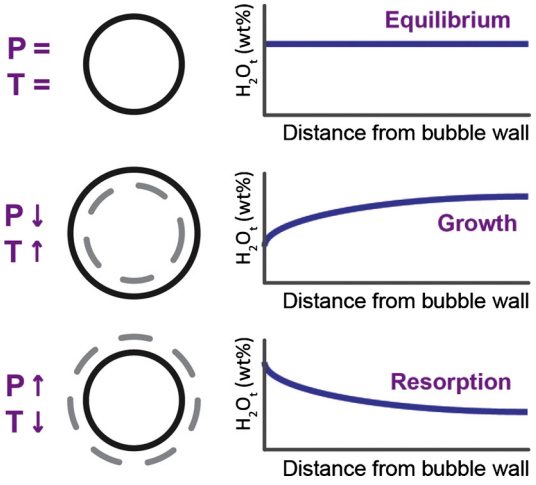

Fig. 1. Bubble growth and resorption. Schematic figure to show the pressure and temperature (P, T) conditions required for a bubble to remain in equilibrium, to grow, or to resorb, with example H_2O_t concentration profiles that result. Solid black lines indicate current bubble size; dashed grey lines indicate previous bubble size, hence whether bubble is growing or resorbing.

scanning electron microscope (BSEM) images (Humphreys et al., 2008) and Fourier-transform infra-red (FTIR) imaging (e.g. Nichols and Wysoczanski, 2007), in order to test this hypothesis.

Two recent studies apply a similar conceptual framework to draw significant conclusions about conduit processes. Watkins et al. (2012) analyse volatile distributions around vesicles in obsidian clasts and find water concentration profiles consistent with bubble resorption (cf. Fig. 1). They infer a pressure increase in the volcanic conduit prior to eruption. Carey et al. (2013) study vesicle distributions in basaltic pyroclasts and find indirect evidence of resorption of bubbles prior to eruption, which they also interpret as evidence of a pressure increase in the conduit. Based on our data, we propose that bubble resorption may occur during the quench from melt to glass as H_2O solubility increases with decreasing temperature, and present an alternative interpretation of these findings in Section 4.4.

Other workers have used textural evidence from experimentally-vesiculated magma samples to investigate interactions between bubbles (Castro et al., 2012). They observe dimpled and sinuous glass films between vesicles, which they interpret as preserved evidence of incipient coalescence of growing bubbles. We analyse water distribution in the same samples and offer an alternative interpretation for their observations, which is consistent with our conceptual model (Section 4.3).

1.1. Water in silicate melts

Interpretation of water distributions in glass relies on quantitative models for water solubility and diffusivity. Experimental studies of various magma compositions show that, for crustal pressures relevant to magmatic degassing, solubility increases with increasing pressure and decreasing temperature (Baker and Alletti, 2012; Newman and Lowenstern, 2002) while diffusivity (D) increases with increasing temperature, decreasing pressure, and increasing water concentration (Ni and Zhang, 2008) (Fig. 2). Temperature exerts a dominant control on water diffusivity and, to a lesser extent, on solubility; however, there remains a gap in data between ambient and magmatic temperatures, which includes the transition between melt and glass.

The two species of water present in glass (H_2O_m and OH) interconvert via the equilibrium reaction

$$H_2O_{m(melt)} + O^o_{(melt)} \rightleftharpoons 2OH_{(melt)}, \quad (1)$$

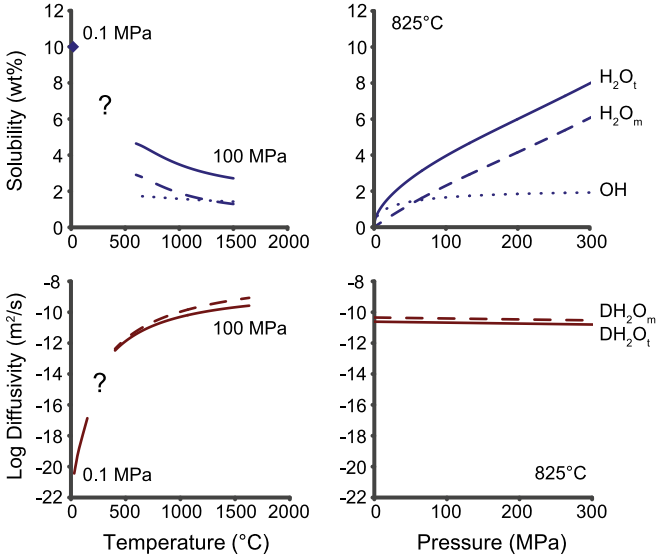

Fig. 2. Controls on diffusivity and solubility of water. Variation in water solubility (upper) and diffusivity (lower) with pressure and temperature for rhyolite composition. A data gap exists between magmatic and ambient temperatures. High-T solubility model is from Newman and Lowenstern (2002) showing proportion of H_2O_m and OH at equilibrium speciation; diffusivity data are from Ni and Zhang (2008) assuming 4 wt% H_2O_t with both H_2O_t and H_2O_m diffusivity shown. Low temperature solubility (diamond) is taken from Anovitz et al. (1999); low temperature diffusivity data (for 0.1 MPa) are from Anovitz et al. (2006).

in which molecular water reacts with bridging oxygens (O°) in the melt to produce hydroxyl groups that are bound to the silicate polymer framework (Stolper, 1982a). The 'total water' (H_2O_t) content of a melt or glass is the sum of the contributions from H_2O_m and OH. The position of the equilibrium of Eq. (1) (the 'equilibrium speciation') changes with pressure, temperature, H_2O_t concentration and melt composition (Hui et al., 2008; Silver et al., 1990; Stolper, 1989, 1982a) (Fig. 2). The bound OH groups are effectively immobile and H_2O_m is the diffusing species; consequently, OH concentration gradients form indirectly by diffusion of H_2O_m and subsequent readjustment towards equilibrium speciation via Eq. (1) (Zhang et al., 1991). For identical conditions, $D_{H_2O_m}$ is therefore higher than $D_{H_2O_t}$ (Fig. 2). At experimental (or magmatic) temperatures the rate of the species interconversion reaction is sufficiently fast that, following a perturbation to the system, equilibrium speciation is re-established over timescales of milliseconds. As a result of the strong temperature-dependence of the reaction rate however, the time taken to achieve equilibrium speciation becomes much longer as temperature decreases, taking minutes to hours at ~600 °C and days at ~400 °C (Zhang et al., 1995, 1991).

2. Materials and methods

Samples are obtained from pre-existing experimental suites, and were manufactured under controlled conditions of pressure (P) and temperature (T). P and T conditions are given in Table 1, along with references to the original studies; sample compositions are given in Table S1 in the Supplementary Information. The experiments were all designed to produce bubble populations with either equilibrium profiles (solubility experiments) or bubble growth profiles (decompression experiments) (Fig. 1).

2.1. Sample production

All samples were synthesised at high pressure (P_{syn}) and temperature (T_{exp}, constant throughout experiment) with excess water to form a starting melt that was water-saturated and fully equili-

Table 1
Sample production details.

Sample		T_{exp} (°C)	P_{syn} (MPa)	P_i (MPa)	Time held at P_i (hr)	P_f (MPa)	dP/dt (MPa/s)	Type of experiment	Expected bubble state at quench	Experimental apparatus
Rhyolite[a] Quench: 3–10 s	ABG1	825	150	100	0.17	100	N/A	Decompression	Equilibrium	Externally-heated pressure vessel; water-cooled rapid quench attachment; 3 mm
	ABG2	825	150	100	0.17	60	0.1	Decompression	Growth	
	ABG6	825	150	100	0.17	80	0.1	Decompression	Growth	
	ABG14	825	150	100	0.25	80	0.5	Decompression	Growth	
	ABG15	825	150	100	0.25	60	0.5	Decompression	Growth	
Phonolite[b] Quench: 3–10 s	IS14	1050	200	200	N/A	100	0.024	Decompression	Growth	Internally-heated pressure vessel; Ar-cooled rapid quench attachment; 5 mm
Rhyolite[c] Quench: 30–60 s	MCN13	825	80	80	72	80	N/A	Solubility	Equilibrium	Externally-heated pressure vessels, quenched using compressed air then submersion in water; 4 mm
Rhyolite[d] Quench: 3–10 s	MCN15	825	80	80	73	56	0.4[†]	Decompression	Growth	Externally-heated pressure vessel; water-cooled rapid quench attachment; 2 mm

Abbreviations: T_{exp} is experimental temperature, P_{syn} is pressure of sample synthesis, P_i is intermediate pressure (if initial step decompression used to nucleate bubbles), P_f is final pressure (NB quench is isobaric), dP/dt is decompression rate. Experimental apparatus column summarises key details, including sample capsule diameter (given in mm). Quench time is estimated and varies with experimental quench apparatus used. Since all experiments were conducted isothermally, expected bubble state at quench is determined by pressure history only.
Sample source:
[a] Burgisser and Gardner (2005).
[b] C.I. Schipper (unpublished), composition as in Iacono Marziano et al. (2007), experimental apparatus as in Di Carlo et al. (2006).
[c] J.F. Larsen (unpublished), experimental apparatus as in Larsen (2008).
[d] J.F. Larsen (unpublished), experimental apparatus as in Larsen et al. (2004).
[†] Sample was decompressed to P_f at 4 MPa/s, then held at P_f for 60 s before quenching.

brated. For decompression experiments, some samples then underwent a single step decompression to a lower intermediate pressure (P_i) to nucleate bubbles and were held at P_i for some time to create a bubble population in equilibrium with the melt prior to further controlled decompression to the final pressure (P_f); for samples without a separate nucleation step (e.g. IS14) decompression began at $P_i = P_{syn}$. For MCN13, an undecompressed sample from a solubility experiment, pressure was constant throughout, i.e. $P_{syn} = P_i = P_f$. All samples were quenched isobarically at P_f; samples were quenched immediately upon reaching P_f except for sample MCN15, which was held at P_f for 60 s before quenching. Experimental quench rates were not directly measured but are estimated to vary from ~3 to ~60 s to the glass transition temperature (Table 1). Full production details for ABG samples are found in Burgisser and Gardner (2005). IS14 was produced following the procedure of Di Carlo et al. (2006); MCN13 following the procedure of Larsen (2008) and MCN15 following the procedure of Larsen et al. (2004).

2.2. Quantifying water content

H_2O_t data are obtained following Humphreys et al. (2008): SIMS H_2O_t analyses are used to calibrate greyscale values in BSEM images of the same area (Fig. 3a, b).

2.2.1. BSEM imaging

Samples were prepared by embedding in epoxy resin and grinding to expose a flat surface. Additional resin was then added to the surface to fill in exposed vesicles and reduce topographic effects during SEM imaging. Re-grinding down to the original exposed surface creates a flat surface of exposed glass and infilled vesicles. Surface topography following sample preparation was checked via confocal microscopy at the National Physical Laboratory using an Olympus LEXT OLS4000 microscope (Wertheim and Gillmore, 2014). The join between the glass and infilling resin is smooth with typically less than 1 μm difference in height between glass and resin, with no gradient in the slope of the glass approaching

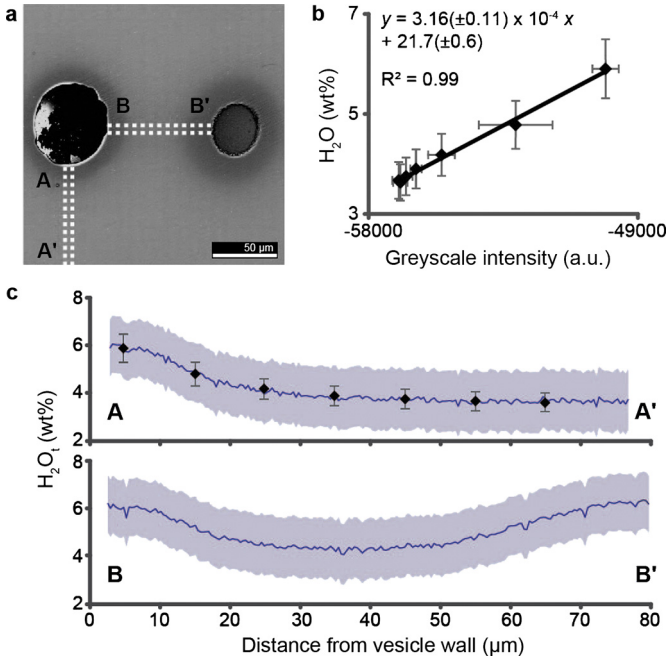

Fig. 3. Extraction of H_2O_t data using SIMS-calibrated BSEM. (a) BSEM image of vesicles in phonolite glass showing dark water-rich halos. Note thin bright white edge effect at vesicle walls. (b) Calibration of SIMS H_2O_t data from profile A–A′ with corresponding BSEM greyscale intensity values. Errors shown result from errors on SIMS H_2O_t analyses (y-axis, ~±10% relative) and errors on mean greyscale value of the profile segments due to noise in the BSEM image (x-axis, one standard deviation from the mean). (c) Profile A–A′ shows H_2O_t measured by SIMS (diamonds) and high spatial resolution H_2O_t concentrations extracted from calibration of greyscale values (solid line). Shading shows error resulting from the calibration equation shown in (b). Profile B–B′ shows H_2O_t data extracted from greyscale values using the calibration equation derived from A–A′.

the vesicle edge. 'Edge effects' (Newbury, 1975) are thus confined to thin (<2 μm) bright white rims at vesicle boundaries. As an additional measure to rule out a topographic cause for greyscale

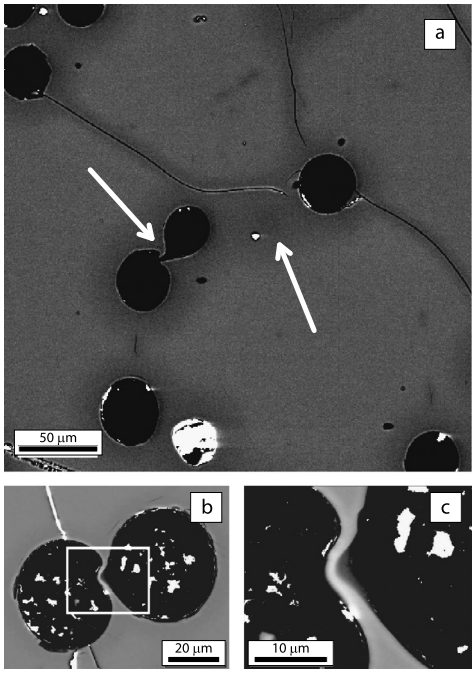

Fig. 4. Resorption profiles and textures. BSEM image of ABG sample. (a) Dark, water-rich halos surround vesicles. Circular dark patch between vesicles (right arrow) is a 'ghost' bubble, i.e. the water-rich halo of a bubble above or below the plane of view. Margins of dark, water-rich glass also seen along cracks but with smaller width than water-rich halos. Cracks extend between vesicles but often terminate at the edge of water-rich halos. (b) Melt films between neighbouring vesicles are often deformed (box is enlarged in (c)). Left arrow in (a) shows broken buckled film. Note that contrast has not been adjusted to highlight halos in (b) and (c). Bright patches are gold-coat remnants or Fe–Ti oxides. Textures are discussed in Section 4.3.

variations approaching vesicle edges and crack margins, the sample stage was rotated and the same area imaged in a different orientation with respect to the incident electron beam and detector. Greyscale variations caused by sample topography (analogous to shadows in a photograph) would be reversed when the sample was rotated by 180°; the consistency of the greyscale variations observed here, irrespective of sample orientation, demonstrates that our results are not affected by sample surface topography. In some images taken after SIMS analysis, residual gold coat remains in cracks and vesicle interiors and appears bright white in BSEM (e.g. Fig. 3a). Images were acquired at Durham University (GJ Russell Microscopy Facility) with a Hitachi SU-70 Analytical High Resolution SEM with attached Gatan Mono CL and associated DigitalMicrograph software using a 15 keV electron beam in backscatter mode with a working distance of 15 mm. Qualitative H_2O_t variations are seen in greyscale variations: dark glass is H_2O_t-rich and light glass is H_2O_t-poor (Fig. 3a, Fig. 4a).

2.2.2. SIMS analysis

Samples were prepared as for BSEM work. $^{1}H^{+}$, $^{23}Na^{+}$ and $^{28}Si^{+}$ were analysed in radial profiles towards vesicles using a CAMECA ims-4f ion microprobe at the Edinburgh Ion Microprobe Facility. A 10.7 keV, 6 nA, O^{-} primary beam was accelerated onto the sample with a net impact energy of 15 keV. Positive secondary ions were accelerated to 4.25 keV and collected sequentially on the electron multiplier detector, using a 75 eV offset with a 40 eV energy window. Profiles were run in scan mode with a 5 μm step size, with each analysed spot approximately 5 × 5 μm and <3 μm deep. H_2O_t concentration was calculated from a working curve of $^{1}H^{+}/^{28}Si^{+}$ which was calibrated twice daily using well constrained standards of varying SiO_2 and H_2O_t content. Errors are ±10% relative.

2.2.3. SIMS-BSEM calibration and data processing

Following the technique of Humphreys et al. (2008), SIMS H_2O_t data were used to calibrate BSEM images in order to extract quantitative H_2O_t data at high spatial resolution (<1 μm). Greyscale values were extracted along a 5 μm-wide profile immediately adjacent to the visible SIMS track, using Gatan DigitalMicrograph software. Mean greyscale values of 5 μm segments were plotted against the corresponding SIMS measurements (Fig. 3). A linear regression fit was applied and the resulting calibration equation used to extract quantitative data in the same image, each new image requiring a separate calibration. 'Edge effects' at vesicle walls are narrow and anomalously bright and thus easily removed from extracted profiles; presented profiles therefore begin a few microns from the vesicle wall. Presented images are enhanced to make greyscale variations more apparent by varying brightness, contrast and gamma settings; these settings do not alter the raw greyscale values used for calibration and data extraction.

For each sample, multiple radial profiles were extracted around multiple vesicles. Once all extracted greyscale data were converted to H_2O_t data using the relevant image calibration equation they were compiled to create a composite dataset of H_2O_t as a function of distance from vesicle wall for the sample. An example figure which shows this profile-averaging methodology is presented in Supplementary Information. The mean H_2O_t value was calculated for all data within 2 μm segments; these mean values form the H_2O_t profile for each sample. Errors shown are twice the standard error of this mean. Averaging all extracted profiles for one sample thus accounts for the variation resulting from vesicles that are sectioned at different distances from their equator (which affects the profile gradient, with steepest profiles for those sectioned directly at the equator, see Supplementary Information), and for variation in H_2O_t resulting from the use of multiple SIMS tracks per sample (which affects the position on the y-axis but not the shape of the profile).

2.2.4. FTIR analysis

Samples were prepared as free-standing wafers polished on both sides. Their high H_2O_t contents required thin wafers (<20 μm) to avoid saturating the detector. Samples were mounted on a glass slide with Crystalbond 509 and ground with silica carbide grit before polishing with 3 μm and 1 μm diamond paste to produce a flat, polished surface. Samples were then flipped and remounted polished side down and ground and polished from the other side. Thickness was monitored during polishing using a micrometer on the glass surface. As target thickness was approached, micrometer measurements were conducted on the adjacent crystalbond to avoid damaging the delicate sample. Final thickness was determined using interference fringes on reflectance FTIR spectra. Samples were finally removed from the slide by dissolving the crystalbond with acetone, then a paintbrush (rather than tweezers) was used to remove the fragile wafers from the acetone bath.

FTIR analyses were acquired at the Institute for Research on Earth Evolution (IFREE), Japan Agency for Marine-Earth Science and Technology (JAMSTEC), using the Varian FTS Stingray 7000 Micro Imager Analyzer spectrometer with an attached UMA 600 microscope. Mid-IR (6000–700 cm^{-1}) transmittance spectroscopic images were collected over 512 scans at a resolution of 8 cm^{-1} using a heated ceramic (globar) infra-red source, a Ge-coated KBr beamsplitter, and the Varian Inc. Lancer Focal Plane Array (FPA) camera housed in the microscope, which consists of a liquid-nitrogen cooled infrared photovoltaic $HgCdTe_2$ (MCT) array detector. The array detector is comprised of 4096 channels (arranged 64 × 64) across a 350 × 350 μm area giving a channel, or spectral, resolution of 5.5 × 5.5 μm. The FPA camera was calibrated regularly. Samples were placed on a KBr window under N_2 purge and areas were selected for analysis using the microscope. Initially a background im-

Table 2
SIMS-calibrated BSEM data and comparison with expected solubilities and diffusivities.

Sample	Experimental observations			Comparison with expected solubilities and diffusivities					
	$H_2O_{t,wall}$ (wt%)[a]	$H_2O_{t,far}$ (wt%)[a]	Half-fall distance (μm)[a]	H_2O_{eq} at T_{exp}, P_f (wt%)	P_{nec} (MPa)	T_{nec} (°C)	H_2O_{eq} at 600 °C, P_f (wt%)	$D_{H_2O_m}$, $D_{H_2O_t}$ at T_{exp}, P_f, H_2O_{eq} at T_{exp}, P_f (m^2/s)[b]	$D_{H_2O_m}$, $D_{H_2O_t}$ at 400 °C, P_f, Half-fall H_2O_t (m^2/s)[b]
ABG1	5.37 (*0.097*)	4.27 (*0.056*)	12 (*9–13*)	3.96	~170	<600	4.64	3.87×10^{-11}, 2.07×10^{-11}	1.78×10^{-12}, 1.45×10^{-12}
ABG2	3.82 (*0.041*)	3.28 (*0.023*)	7 (*5–8*)	2.95	~90	<600	3.71	2.36×10^{-11}, 1.11×10^{-11}	2.40×10^{-13}, 1.85×10^{-13}
ABG6	4.86 (*0.031*)	4.29 (*0.040*)	5 (*5–7*)	3.48	~140	<600	4.22	3.07×10^{-11}, 1.55×10^{-11}	8.86×10^{-13}, 7.12×10^{-13}
ABG14	5.46 (*0.044*)	4.92 (*0.055*)	4 (*3–4*)	3.48	~170	<600	4.22	3.07×10^{-11}, 1.55×10^{-11}	2.42×10^{-12}, 1.99×10^{-12}
ABG15	4.04 (*0.037*)	3.71 (*0.031*)	8 (*7–9*)	2.95	~100	<600	3.71	2.36×10^{-11}, 1.11×10^{-11}	6.02×10^{-13}, 4.78×10^{-13}
IS14	6.50 (*0.079*)	4.47 (*0.047*)	12 (*11–13*)	3.61	>250	<950	–	–, $\sim 1 \times 10^{-10}$	–, –
MCN13	4.64 (*0.059*)	3.47 (*0.050*)	10 (*10–11*)	3.48	~130	<600	4.22	3.07×10^{-11}, 1.55×10^{-11}	5.14×10^{-13}, 4.07×10^{-13}

Abbreviations: $H_2O_{t,wall}$ is H_2O_t measured at vesicle wall, $H_2O_{t,far}$ is minimum H_2O_t in far-field, H_2O_{eq} is equilibrium H_2O_t solubility for given P, T conditions, P_{nec} is pressure necessary to explain observed $H_2O_{t,wall}$ at T_{exp}, T_{nec} is temperature necessary to explain observed $H_2O_{t,wall}$ at P_f, $D_{H_2O_m}$ and $D_{H_2O_t}$ are diffusivities of H_2O_m and H_2O_t. Notes: H_2O_{eq}, P_{nec} and T_{nec} from solubility model of Newman and Lowenstern (2002) for rhyolite composition (lower T limit of model: 600 °C), from experimental data of Iacono Marziano et al. (2007) for phonolite (valid 30–250 MPa, 950–1050 °C).

[a] Measurement errors given in brackets. SIMS-calibrated BSEM errors given as twice standard error of the mean sample profile, errors on half-fall distance represent range of values obtained when error in H_2O_t value is propagated.

[b] Calculated using diffusivity model of Ni and Zhang (2008) for rhyolites, order of magnitude estimate for phonolite IS14 taken from Iacono Marziano et al. (2007).

age of the KBr window was collected, which was subtracted from the sample image. New background images were taken approximately every 300 min. Images were processed using Varian Win-IR Pro software (v3.3.1.014). Individual spectra for use in transects were extracted from the images and H_2O concentrations were calculated in the normal manner by entering the height (absorbance) of the relevant peak above a linear background into the Beer–Lambert law (Stolper, 1982b). H_2O_t was calculated from the peak at ~3500 cm^{-1} and H_2O_m from the peak at ~1630 cm^{-1}, using respective molar absorptivity coefficients of 90 ± 4 $l\,mol^{-1}\,cm^{-1}$ (Hauri et al., 2002) and 55 ± 2 $l\,mol^{-1}\,cm^{-1}$ (Newman et al., 1986). OH values were calculated by subtracting calculated H_2O_m from H_2O_t. Sample density was calculated iteratively from major element compositions (Lange and Carmichael, 1987) and H_2O_t content (Ochs III and Lange, 1997). Sample thicknesses for spectra along the transects were determined using the frequency of interference fringes on reflectance spectra (e.g. Nichols and Wysoczanski, 2007). Images were collected in reflected light of exactly the same area that had been analysed in transmitted light, and spectra at the same coordinates were extracted and processed. A refractive index of 1.5 (Long and Friedman, 1968) was used for rhyolite. Errors on sample thickness determinations are ±3 μm (Nichols and Wysoczanski, 2007). Since thickness measurements for transect spectra all fall within 3 μm of each other with no systematic variation along transect, the average sample thickness along the transect was used when processing each spectrum. FTIR images are output in terms of absorbance. They were converted to concentration by applying the Beer–Lambert law, as above, using the mean sample thickness. Analytical errors are ±15% relative, largely as a result of the relative impact of uncertainties in thickness measurement for thin samples. However, it is important to note that a change in the thickness value used would shift the H_2O_t, H_2O_m and OH profiles up or down on the y-axis, but would not alter their shapes or positions relative to one another. Additional error results from volumetric averaging of concentration variations in 3D. Thin samples relative to vesicle diameter reduce this error but increase the relative importance of errors in thickness measurement; however the ratio of H_2O_m:OH again remains unaffected.

3. Results

We find that all vesicles, in all samples, have higher H_2O_t concentrations adjacent to the vesicle walls than in the far-field (Table 2). In BSEM images, this is seen as a dark halo surrounding each vesicle (Fig. 3a, Fig. 4a). In some areas dark circles are present even where no vesicle is observed on the BSEM image (Fig. 4a). In these instances, optical microscopy shows that vesicles are present just below the sample surface. We conclude that a water-rich shell surrounds each vesicle in 3D, which is seen as a water-rich halo when vesicles are cross-sectioned.

The SIMS-calibrated H_2O_t concentration gradients are steepest at the vesicle wall and decay to a far-field value over a few tens of microns from the vesicle wall (Fig. 5), corresponding to the edge of the observed halos in BSEM images. We quantify halo widths using the half-fall distance, i.e. the distance at which H_2O_t concentration is halfway between the maximum and minimum values along profile (Anovitz et al., 2006) (Table 2, Fig. 5c). To eliminate stereological issues, which arise where a vesicle is not sectioned through its equator (see Supplementary Information), half-fall distance for each sample is calculated using the single vesicle in each sample with the steepest profile, which will be the vesicle cross-sectioned closest to its equator. Concentration profiles caused by bubble resorption will be radially symmetric around the centre of the bubble, which, for the same conditions of resorption, will result in smaller bubbles having steeper profile gradients (hence shorter half-fall distances) than larger bubbles. With the exception of sample IS14 (radius 100 μm), all samples have vesicles of a similar size (radii 16–30 μm) and so their half-fall distances are comparable (see Supplementary Information).

FTIR images of vesicular experimental samples also show higher H_2O_t concentrations around vesicles than in the far-field (Fig. 6). Transects between vesicles show that H_2O_t and H_2O_m concentrations increase towards the vesicle walls in both MCN13, which is an undecompressed solubility sample, and MCN15, which is a decompression sample. By contrast, the OH profile is flat between vesicles in the solubility sample, and is depleted around vesicles in the decompression sample. In the decompression sample, the H_2O_m:OH ratio increases from 1.7 in the far-field to 7.0 at the vesicle wall.

Thin cracks commonly extend between vesicles (Fig. 4a). Many of these cracks do not reach the vesicle walls; instead they terminate as they enter the water-rich halo. BSEM images show that cracks have dark, water-rich margins on either side (Fig. 4a). The width of these water-rich margins is variable but is typically much less than the width of the vesicle halos. The observed width of the water-enriched margin is affected by the angle at which the crack intersects the sample surface, equalling the true width only for cracks intersecting the surface at 90°, and appearing wider with increasing obliquity of the angle of intersection. Observed half-fall distances of water-rich crack margins are therefore upper estimates. In sample ABG1 (shown in Fig. 4a), typical half-fall dis-

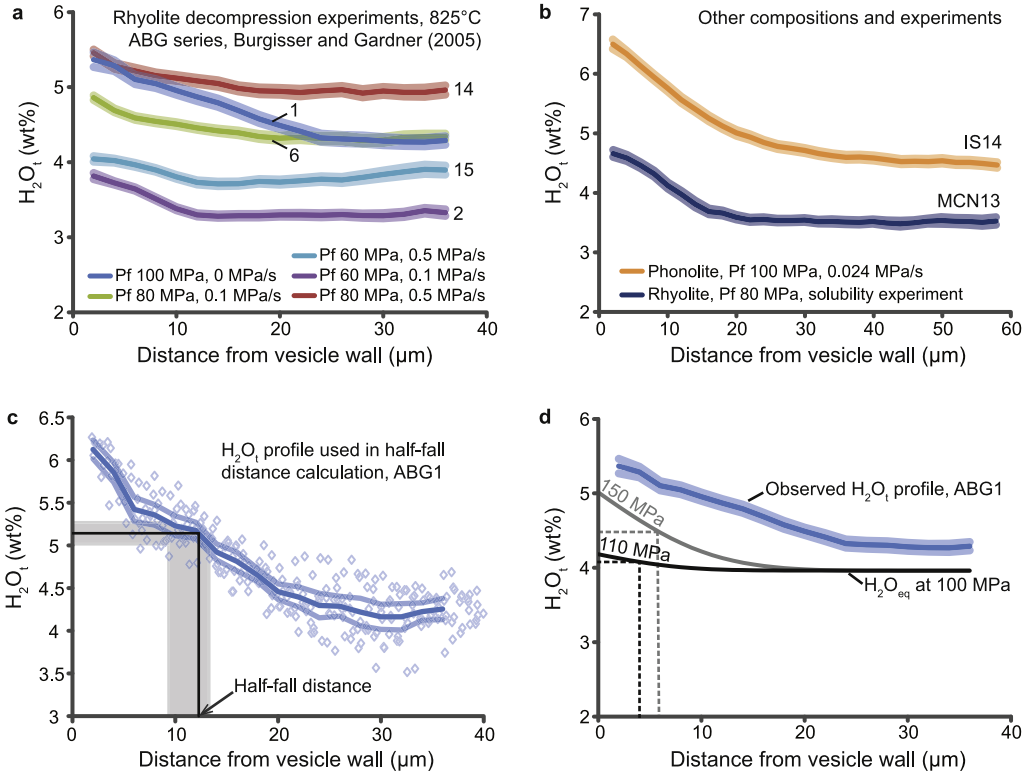

Fig. 5. Resorption profiles. H_2O_t profiles extracted using SIMS-calibrated BSEM for samples listed in Table 1, including both rhyolite and phonolite compositions and decompression experiments (bubble growth expected) and solubility experiments (bubble-melt equilibrium expected). (a) ABG rhyolite series (profiles are labelled with their sample number); (b) IS14 phonolite decompression and MCN13 rhyolite solubility samples. Semi-opaque boundaries indicate twice the standard error of the mean. (c) Calculation of half-fall distance for sample ABG1, which uses the H_2O_t profile of the single vesicle with the steepest gradient (hence the vesicle sectioned closest to its equator). Blue diamonds represent H_2O_t values extracted from SIMS-calibrated BSEM greyscale profiles; semi-opaque boundaries indicate twice the standard error of the mean. Black line shows half-fall H_2O_t concentration (the midpoint between the maximum and minimum values along the profile) and the corresponding half-fall distance. Grey shading shows error on half-fall distance resulting from propagation of error on half-fall H_2O_t concentration (twice the standard error of the mean). (d) Comparison of observed ABG1 H_2O_t profile (blue profile) with profiles expected for resorption caused by pressure fluctuation during the quench process. Profiles were calculated using a 1-D half-space diffusion model assuming a pressure increase of 10 or 50 MPa (black and grey profiles, respectively) lasting 1 s, with $D_{H_2O_t}$ of 2.07×10^{-11} m^2/s (calculated according to Ni and Zhang, 2008 and assuming constant $T_{exp} = 825\,°C$ and $H_2O_t = 3.96$ wt%). Resulting half-fall distances are shown as dashed lines. Pressure fluctuation during quench was observed to be <10 MPa for less than 1 s, and neither this nor a 'worst case' increase of 50 MPa can replicate the observed H_2O_t profile and associated half-fall distance (12 μm, see (c)). (For interpretation of the references to color in this figure legend, the reader is referred to the web version of this article.)

tances of water-rich crack margins are <3 μm, compared with a half-fall distance of 12 μm for the water-rich halos around vesicles (Table 2).

Adjacent vesicles are often separated by sinuous, rather than planar, melt films (Fig. 4b, c). These films are similar to those described by Castro et al. (2012), whose study of vesicular samples included sample ABG1, which is also investigated in this study (Fig. 4, Table 1).

4. Discussion

4.1. Resorption mechanism

In all experiments the pressure history was carefully controlled in order to produce either growing bubbles, or bubbles in equilibrium with the melt (i.e. neither growing nor resorbing), yet all samples have increasing H_2O_t concentrations towards vesicle walls. These concentration profiles are evidence of water diffusion from the bubble/vesicle back into the melt/glass, characteristic of resorbing bubbles (Fig. 1).

We observe resorption around all vesicles in all samples, independent of melt composition, experimental apparatus used or pressure history; this ubiquity implies a common mechanism. We propose that bubble resorption is caused by an increase in the equilibrium solubility of water in the melt (H_2O_{eq}), as a consequence of decreasing temperature during quench.

For all samples the water concentration at the vesicle wall exceeds H_2O_{eq} for the final pressure (P_f) and temperature conditions of the experiment (T_{exp}) immediately prior to quench; in four cases, the concentration even exceeds H_2O_{eq} at the highest pressure of the experiment (P_{syn}). These water concentrations would require an increase in pressure of 30 to 150 MPa under isothermal conditions (Table 2). Melt-gas interfacial tension produces an overpressure within a bubble given by $\Delta P = 2\sigma/r$ where σ is interfacial tension and r is bubble radius. For $\sigma = 0.08$ $N\,m^{-1}$ (Gardner and Ketcham, 2011), the pressure increase above the reported experimental pressure is only 0.03 MPa for a bubble with a 5 μm radius, decreasing to 0.003 MPa for a 50 μm bubble radius. The observed vesicle wall water concentrations can therefore not be explained by interfacial tension effects. Although the quench process is described as isobaric, a small, transient pressure increase may occur during the quench process as the pressure medium re-equilibrates once the sample moves into the quench vessel (e.g. Holloway et al., 1992; Di Carlo et al., 2006). In the ABG and IS14 experiments described here, this fluctuation was observed on the pressure gauge as a pressure increase of <10 MPa lasting for less than one second. Comparison of the observed resorption profiles with the results of diffusion modelling of this transient pressure increase (Fig. 5d) demonstrates that it is far too small to account for the observed vesicle wall water concentrations and half-fall distances, providing strong evidence that resorption is not driven by pressure increase in our samples.

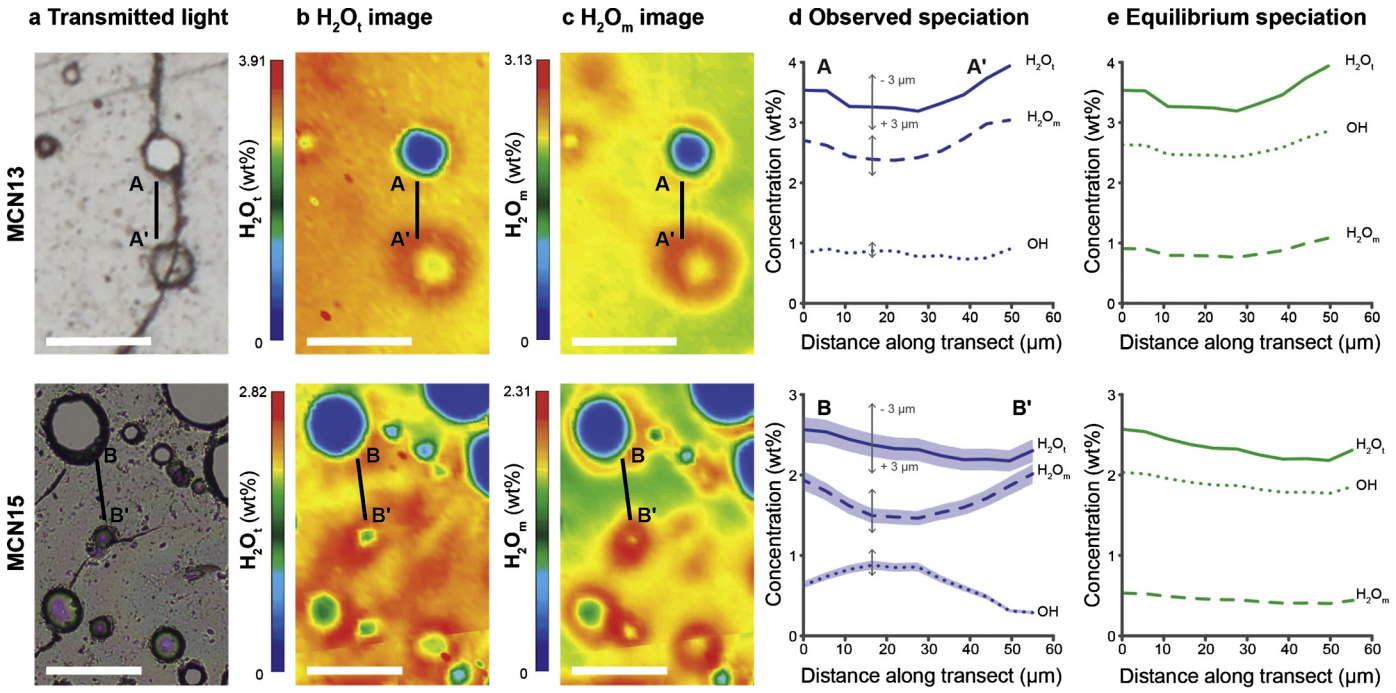

Fig. 6. Water speciation distributions. Top: solubility sample MCN13; bottom: decompression sample MCN15. Panels show (a) transmitted light image of samples and (b) H_2O_t and (c) H_2O_m distributions obtained by FTIR imaging. White bar is 100 μm. Both samples show enrichment in H_2O_t and H_2O_m around vesicles. Panel (d) (blue graph) shows observed H_2O_t, H_2O_m and OH concentrations along highlighted transects between two vesicles. Concentrations were calculated using average thickness along transect. Thickness measured along transect was constant for MCN13 (top), but varied slightly for MCN15 (bottom). This variation was not systematic (i.e. glass did not thin or thicken towards vesicle walls) and had a standard deviation <1 μm. Blue shading shows the resulting error on calculated concentrations and demonstrates that this error cannot explain the observed profile shapes. Grey arrows shown for both samples show the typical change in calculated concentrations assuming a ±3 μm error on the average thickness used. This error would shift the profiles up or down but would not alter their shape or the dominance of H_2O_m relative to OH. Panel (e) (green graph) shows the expected H_2O_m and OH profiles for the observed H_2O_t profiles in (d) assuming equilibrium speciation at the experimental run temperature (T_{exp}), calculated using the relationship of Nowak and Behrens (2001). Comparison of (d) and (e) demonstrates that both samples exhibit higher H_2O_m:OH ratios than expected, with further enrichment in H_2O_m around vesicles. Solubility sample MCN13 shows a flat OH profile, whilst decompression sample MCN15 shows depletion in OH around vesicles. (For interpretation of the references to color in this figure legend, the reader is referred to the web version of this article.)

By contrast, in all samples, the water concentration at the vesicle wall is consistent with H_2O_{eq} expected at P_f for temperatures <600 °C (i.e. interpolated in the solubility data gap, Fig. 2; Table 2). All experiments are conducted isothermally so these temperatures are not reached until the sample is quenched at the end of the experiment. $D_{H_2O_t}$ decreases dramatically with decreasing temperature (Fig. 2) so the observed halos cannot be produced by post-quench hydration at ambient temperatures (at 30 °C $D_{H_2O_t}$ is $\sim 10^{-21}$ m^2/s (Anovitz et al., 2006) and ~30 years would be required to create a 1 μm halo). We conclude that the observed bubble resorption profiles were created rapidly during quench.

This conclusion is further supported by our FTIR data, which show that samples have higher H_2O_m:OH ratios than expected for equilibrium speciation at the experimental temperature (Fig. 6). Although this could be partly attributed to the influence of the 'quench effect', whereby the slowing interconversion reaction can still maintain speciation in equilibrium with the decreasing temperature during the initial stages of quench, this cannot explain the observation that the water-rich halos around vesicles are significantly enriched in H_2O_m (Fig. 6). This enrichment instead indicates disequilibrium speciation, which is evidence that bubble resorption results from a rapid decrease in temperature. During bubble resorption, water enters the melt as H_2O_m (Stolper, 1982a). At magmatic temperatures Eq. (1) acts rapidly to convert some of this additional H_2O_m to OH in order to regain equilibrium speciation. However, during quench, the reaction slows dramatically (Zhang et al., 1995, 1991), so the melt in the resorption halos remains enriched in H_2O_m. If resorption were driven by a pressure increase at experimental/magmatic temperatures, the rate of the species interconversion reaction would be sufficiently rapid that water species would be in equilibrium; hence speciation data provide additional evidence that resorption is not driven by pressure increase in our samples.

The breakdown of the interconversion reaction over rapid quench timescales means that the diffusion of resorbing H_2O_m is not slowed by conversion to immobile OH; consequently, quench resorption is controlled by $D_{H_2O_m}$, which is always greater than $D_{H_2O_t}$ (Fig. 2). A more profound consequence is that OH concentrations in the melt are largely unaltered by bubble resorption if quench is sufficiently rapid. Fig. 6 shows the distribution of water species for two samples: MCN13 is from a solubility experiment and is expected to have had a flat, equilibrium water profile (Fig. 1) prior to quench; MCN15 is from a decompression experiment and is expected to have had a bubble growth profile (water depletion adjacent to bubbles, Fig. 1) prior to quench. Whilst both samples show enrichment in H_2O_m around vesicles, MCN13 shows a flat OH profile, and MCN15 shows depletion in OH adjacent to vesicles. We conclude that rapid quench preserves the OH profile created prior to quench. This record of pre-quench conditions, preserved in the OH distribution, may be accessed via FTIR.

4.2. Controls on quench resorption

Isobaric resorption of water is controlled by the thermal history of the sample during quench. The dependence of water solubility and diffusivity on temperature is strong, non-linear, and incompletely characterised (note gaps in Fig. 2), precluding quantitative modelling of quench resorption. Nonetheless, our data yield valuable insights into the physical controls on the process.

Samples ABG1 and MCN13 have similar, rhyolitic composition and both are expected to be in equilibrium (*sensu* Fig. 1) prior to quench. MCN13 has the same half-fall distance as ABG1 (within

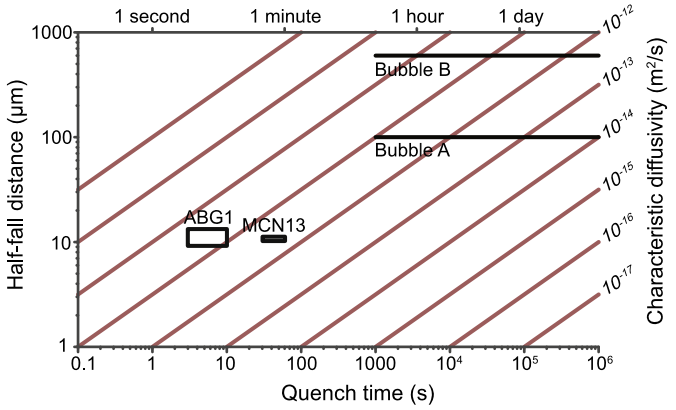

Fig. 7. Relationship between quench time, characteristic diffusivity and half-fall distance. Boxes encapsulate measured half-fall distances (with error) of samples with estimated quench time for equilibrium samples ABG1 (3–10 s) and MCN13 (30–60 s). Half-fall distances from Watkins et al. (2012) samples (Bubbles A and B, black lines) show range of possible characteristic diffusivity and quench time that could explain them.

error). However, its lower H_2O_t content should give lower $D_{H_2O_m}$, and therefore a smaller half-fall distance than ABG1 (Figs. 5, 7). We attribute this to its slower quench (estimated 30–60 s to glass transition for MCN13, cf. 3–10 s for ABG1; see Appendix A for methodology) giving more time for resorption at high temperature, where diffusivity is high.

The five ABG samples have identical compositions and quench histories, but differ in decompression histories. The half-fall distance for the undecompressed, equilibrium sample (ABG1) is considerably longer than for the decompressed samples (Table 2). We propose that this difference reflects their different pre-quench water distributions. A flat (equilibrium) pre-quench profile is expected for ABG1, whilst the other samples' pre-quench profiles should be depleted at the bubble wall as a result of decompression-induced bubble growth (Fig. 1). For the same quench history, therefore, water is expected to diffuse furthest in sample ABG1 since there is no pre-quench, water-depleted (hence low diffusivity) region to 'fill in' near the bubble wall.

We determine a 'characteristic diffusivity', $D_{H_2O_{ch}}$, for sample ABG1 from the observed half-fall distance (L) and the timescale over which the diffusion occurs (t), by rearranging $L = \sqrt{D_{H_2O_{ch}} t}$. This is a form of the half-fall distance derived for 1D Fickian diffusion (i.e. in a plane half-space) and is valid for constant diffusivity and with boundary conditions of constant H_2O concentration (e.g. Anovitz et al., 2004). In these samples however, both diffusivity and solubility vary as a function of time as the sample cools during the quench process, and so $D_{H_2O_{ch}}$ represents a time-integrated 'average' diffusivity over the duration of resorption/hydration. Since the cooling history of the samples is calculated (Appendix A) rather than directly measured, we calculate $D_{H_2O_{ch}}$ for ABG1 using both the upper and lower estimates of quench time (3–10 s, see Table 1). 3 s is likely to be an underestimate of the true diffusion timescale over which the profile forms, but is representative of previous assumptions of the time to the glass transition for these samples (Burgisser and Gardner, 2005; Castro et al., 2012). The evidence of minor H_2O enrichment around cracks shows that some diffusion also occurs below the glass transition, and so an upper limit of 10 s is also used, based on the time for the sample to cool to 300 °C. Although diffusivity data below 400 °C requires extrapolation of the Ni and Zhang (2008) diffusivity model beyond its temperature range, doing so suggests that diffusivity decreases a further order of magnitude between 400 and 300 °C, requiring 10 s to form a 1 μm hydration lengthscale. Since the sample spends only ~1 s in the temperature range 310–290 °C, profiles are not expected to be significantly modified below 300 °C. Accordingly, for ABG1 we calculate $D_{H_2O_{ch}}$ as $\sim 6 \times 10^{-11}$ m^2/s to $\sim 8 \times 10^{-12}$ m^2/s, for 3 to 10 s respectively. Comparison with computed values of $D_{H_2O_m}$ for this sample (following Ni and Zhang, 2008) of 4×10^{-11} m^2/s at T_{exp} and 2×10^{-12} m^2/s at 400 °C (Table 2), indicates that the bulk of the resorption occurs at high temperature; i.e. during the early part of the quench.

4.3. Resorption textures and the glass transition

Textural observations indicate that resorption occurs largely above the melt's glass transition temperature T_g. Most samples contain cracks with thin water-rich margins (Fig. 4). The cracks must form below T_g so the margins of cracks indicate that at least some hydration occurs into glass, rather than melt. However, the margins of cracks typically extend into the glass less than half as far as the resorption halos around vesicles; furthermore, the cracks often terminate in the outer part of the resorption halos.

A melt's T_g varies with its water content and quench rate (Hui and Zhang, 2007). For ABG samples, we calculate $T_g \sim 460$ °C in the far-field (typically 4 wt% water), and $T_g \sim 430$ °C at the vesicle wall (typically 5 wt% water) (see Appendix A for methodology). Consequently, during quench, melt in the far-field is capable of cracking whilst the more water-rich melt near the bubbles is still plastic. Our textural observations are, therefore, consistent with early resorption of water around bubbles during quench, transition to glass of the melt in the far-field, cracking of the glass, followed, finally, by minor hydration of the crack margins during cooling to ambient temperature.

When resorption occurs above the glass transition, bubbles can shrink. Integrating under the water concentration profile for ABG1 we calculate that 40% by mass of the water that was in the bubble pre-quench is resorbed into the melt during cooling (see Supplementary Information). If we assume, for purposes of illustration, that this resorption is compensated exactly by a loss of bubble volume of 40%, then the observed sample porosity would be only 60% of the pre-quench value. This is likely to be an overestimate of the volume change caused by resorption since it assumes that all excess H_2O in the surrounding halo was derived from the bubble while it was still able to resorb, whereas the evidence of hydrated crack margins suggests that at least some of this diffusion happened below T_g. Similarly it is possible that, as T_g is approached, the increasing structural relaxation timescale of the melt with cooling may make it difficult for the reduction in bubble volume to keep pace with the loss of internal H_2O vapour. However, this calculation does not account for the additional change in bubble volume that would occur due to simple thermal contraction of the H_2O vapour. If this is included (see Supplementary Information) then the observed sample porosity could be as little as 30% of the original pre-quench porosity.

Possible evidence for significant reduction in bubble volumes can be seen in the deformed films that exist between neighbouring vesicles (Fig. 4b, c). Films that stretch as adjacent bubbles grow and interact will not remain planar if the bubbles subsequently shrink, but will tend to buckle. These features have previously been interpreted as evidence of novel bubble coalescence mechanisms at high pressure (Castro et al., 2012). In the light of our findings, we reinterpret these textures as evidence of resorption-driven bubble shrinkage during quench.

4.4. Interpretation of natural samples

This study demonstrates that water resorption should be expected whenever vesicular magma quenches. The degree of resorption will vary considerably with diffusivity and quench conditions and will be most significant where D_{H_2O} (particularly $D_{H_2O_m}$) is

high and quench is slow (Fig. 7). If magma has undergone significant degassing during ascent, low residual H_2O contents will result in lower D_{H_2O} and higher melt viscosity; hence, if such a melt is rapidly quenched (e.g. in an eruption column), then quench resorption is unlikely to be significant. Where erupted material cools more slowly there is potential for significant resorption even for melts with low H_2O contents. Quench resorption affects both glass transition temperature and vesicularity, and may therefore be important in processes such as the welding of ignimbrites, the formation of rheomorphic flows, and the formation of obsidian. The samples described in this study were quenched rapidly at high pressure and may have natural analogues in submarine and subglacial eruptions, where magma is erupted at higher than ambient pressure and is therefore likely to have higher H_2O contents and correspondingly greater potential for resorption. We stress that bubble resorption may also result from a pressure increase; however, since both temperature and pressure usually drop dramatically through eruption, we propose that the quench mechanism developed in this study will usually provide the most straightforward explanation when evidence of resorption in natural magmatic products is found.

Watkins et al. (2012) describe resorption profiles around vesicles in obsidian clasts from the ca. 1340 AD eruption of Mono Craters, California and propose that resorption was caused by a pressure increase of ~10 MPa in the volcanic conduit prior to eruption. We note that a temperature decrease to ~600 °C, which must occur during quench, is also sufficient to explain the observed H_2O_t concentrations at vesicle walls (Liu et al., 2005; Newman and Lowenstern, 2002).

Watkins et al. (2012) discount thermal resorption as inconsistent with a secondary vesicle population that they observe in the water-rich resorption halo around one vesicle, arguing that high melt viscosity at temperatures near the glass transition would preclude secondary bubble nucleation. By contrast, we interpret this observation as evidence of cooling and reheating of this sample. This is consistent with previous studies that use geospeedometry to interpret similar obsidian clasts, from the same locality, as fragments from chilled conduit margins that were subsequently entrained by erupting magma (Newman et al., 1988; Stolper, 1989; Zhang et al., 2000, 1997, 1995). Water-rich glass in the resorption halo produced by the first cooling event would be prone to secondary vesiculation on reheating. Consequently, we conclude that repressurization is not required to explain the observations of Watkins et al.; rather, we propose that their observations could provide a natural counterpart to our experimental observations.

Carey et al. (2013) observe similar secondary populations of vesicles in basaltic pyroclasts from explosive activity of Kilauea (Hawai'i) in 2008. They propose that repressurization of magma during convection in a lava lake produces a water-rich halo around bubbles which subsequently vesiculates during eruption; a thermal origin is not considered, but our results indicate that it is a plausible alternative.

Secondary vesicle populations like those observed by Watkins et al. (2012) and Carey et al. (2013) are evidence of a fluctuation in either pressure or temperature conditions (or both) but do not, by themselves, reveal which occurred. Our observations of quench resorption highlight the need to consider variation in temperature, as well as pressure, when evidence of bubble resorption is found. Our FTIR results indicate that water speciation data provide a methodology for distinguishing between these two mechanisms when interpreting natural samples. Quench resorption creates dramatically increased H_2O_m:OH ratios around bubbles because the interconversion reaction (Eq. (1)) cannot maintain equilibrium speciation as the sample cools. By contrast, pressure-driven resorption at magmatic temperatures would yield H_2O_m:OH ratios consistent with equilibrium speciation. Consequently, any analytical technique that can quantify water species with high spatial resolution could be used to distinguish between resorption mechanisms.

5. Conclusions and implications

We show that bubble resorption is a ubiquitous consequence of the increase in H_2O solubility during magma cooling. We also show that resorption occurs mainly above the glass transition, whilst the melt is still plastic and the bubbles are able to respond by shrinking. We observe buckled melt films between vesicles in our samples, which we interpret as direct evidence of bubble shrinkage.

Our FTIR data show that the resorption signal is dominated by H_2O_m, whilst the OH distribution records pre-quench conditions. The different behaviour of the water species is a consequence of their different diffusivities, and the kinetics of their interconversion reaction. Our work provides the conceptual underpinning for an analytical technique that allows both pre-quench processes, such as bubble growth, and post-eruptive quench to be interrogated. With further experimental work to fill the gap in our knowledge of water diffusivity and solubility around the glass transition temperature (Fig. 2), this should provide a quantitative tool for reconstructing both the pre- and post-eruptive history of natural samples.

The ubiquity of quench resorption has broad implications. Studies that use the final vesicle size or volume fraction of experimental or natural samples to make inferences about bubble growth, degassing mechanisms or eruptive processes may need to be revised to account for bubble shrinkage during resorption; SIMS-calibrated BSEM images represent a simple and effective way to do so. Similarly, studies that make inferences from measurement of bulk dissolved water content or speciation of vesicular samples (e.g. solubility experiments, geospeedometry) should assess for quench resorption and disequilibrium speciation. Finally, the role that bubble resorption during cooling of eruptive products may play in promoting rheomorphic flow, welding of ignimbrites and the formation of obsidian is worthy of further investigation.

Author contributions

I.M.M. collected and processed SEM, SIMS and FTIR data. A.R.L.N. assisted with FTIR sample preparation and analysis, and undertook additional FTIR data processing. A.B., C.I.S. and J.F.L. performed decompression and solubility experiments. I.M.M., E.W.L. and M.C.S.H wrote the paper. All authors discussed the results and commented on the manuscript.

Research Data Access Statement

The data underlying this study are available from the corresponding author.

Acknowledgements

We thank R. Hinton and J. Craven for SIMS assistance at the Edinburgh IMF, L. Bowen for SEM training and support at the GJ Russell Microscopy Facility at Durham University, and D. Wertheim and G. Gillmore for undertaking sample imaging with confocal microscopy at the NPL. The JSPS Summer Program provided financial support to enable I.M.M. to visit Japan. SIMS data acquisition was funded by NERC IMF award IMF455/1011. I.M.M was supported by NERC PhD Studentship NE/H524606/1. M.C.S.H. is supported by a Royal Society University Research Fellowship. A.B. and C.I.S. acknowledge support from ERC grant 202844 under the European

FP7. We thank A. Proussevitch and C. Martel for their detailed and constructive reviews and Tim Elliott for editorial handling.

Appendix A. Calculating T_g

The glass transition temperature (T_g) represents the transition between regimes where a material behaves like a glass (elastic response to stress) and where it behaves as a fluid (viscous response to stress) (Dingwell and Webb, 1990). This transition is effectively governed by the structural relaxation timescale of the silicate melt, and is therefore dependent on thermal history amongst other factors (Dingwell and Webb, 1989; Giordano et al., 2005). Viscosity and T_g are linked empirically for hydrous rhyolite containing 6 ppm to 8 wt% H_2O_t by the relationship: η at $T_g = 10^{11.45}/q$; where η is viscosity in Pa s and q is quench rate at T_g in K/s (Zhang et al., 2003). Temperature–time history was not measured during sample quench and therefore the cooling rate at T_g is not directly known, but the cooling rate is expected to be strongly non-linear over time during quench. Following the model of Xu and Zhang (2002) for sample quench in water, we estimate both temperature T_{sample} and cooling rate as a function of time for our samples during quench. For each timestep, we use the cooling rate to calculate the apparent viscosity at T_g using the relationship of Zhang et al. (2003) above. We then calculate the nominal temperature (T_n) required to give this apparent viscosity, based on the H_2O_t-dependent viscosity model of Hui and Zhang (2007) for each timestep. At the glass transition, $T_n = T_g = T_{sample}$. This is identified graphically by plotting T_n and T_{sample} for each timestep, where the intersection of the two curves gives the T_g of the sample, as well as the approximate time in which it is reached.

Thus a typical, rapidly-quenched rhyolite sample containing 4 wt% water has a T_g of ~460 °C which is reached in ~4 s, whereas a sample containing 5 wt% water has a T_g of ~430 °C which is reached in ~5 s. While this method has a large error (±40 °C) in the absolute value of T_g, the relative variation of T_g with water content is more robust, highlighting the effect of water content on T_g and the time taken to cross the glass transition during quench.

Appendix B. Supplementary material

Supplementary material related to this article can be found online at http://dx.doi.org/10.1016/j.epsl.2014.05.037.

References

Anovitz, L.M., Elam, J.M., Riciputi, L.R., Cole, D.R., 1999. The failure of obsidian hydration dating: sources, implications, and new directions. J. Archaeol. Sci. 26, 735–752.

Anovitz, L.M., Elam, J.M., Riciputi, L.R., Cole, D.R., 2004. Isothermal time-series determination of the rate of diffusion of water in Pachuca obsidian. Archaeometry 46, 301–326.

Anovitz, L.M., Riciputi, L.R., Cole, D.R., Fayek, M., Elam, J.M., 2006. Obsidian hydration: a new paleothermometer. Geology 34, 517.

Baker, D.R., Alletti, M., 2012. Fluid saturation and volatile partitioning between melts and hydrous fluids in crustal magmatic systems: the contribution of experimental measurements and solubility models. Earth-Sci. Rev. 114, 298–324.

Burgisser, A., Gardner, J.E., 2005. Experimental constraints on degassing and permeability in volcanic conduit flow. Bull. Vulcanol. 67 (1), 42–56.

Carey, R.J., Manga, M., Degruyter, W., Gonnermann, H., Swanson, D., Houghton, B., Orr, T., Patrick, M., 2013. Convection in a volcanic conduit recorded by bubbles. Geology 41, 395–398.

Castro, J.M., Burgisser, A., Schipper, C.I., Mancini, S., 2012. Mechanisms of bubble coalescence in silicic magmas. Bull. Volcanol. 74, 2339–2352.

Di Carlo, I., Pichavant, M., Rotolo, S.G., Scaillet, B., 2006. Experimental crystallization of a high-K arc basalt: the golden pumice, Stromboli Volcano (Italy). J. Petrol. 47, 1317–1343.

Dingwell, D.B., Webb, S.L., 1989. Structural relaxation in silicate melts and non-Newtonian melt rheology in geologic processes. Phys. Chem. Miner. 16, 508–516.

Dingwell, D.B., Webb, S.L., 1990. Relaxation in silicate melts. Eur. J. Mineral. 2, 427–449.

Gardner, J.E., Ketcham, R.A., 2011. Bubble nucleation in rhyolite and dacite melts: temperature dependence of surface tension. Contrib. Mineral. Petrol. 162, 929–943.

Giordano, D., Nichols, A.R.L., Dingwell, D.B., 2005. Glass transition temperatures of natural hydrous melts: a relationship with shear viscosity and implications for the welding process. J. Volcanol. Geotherm. Res. 142, 105–118.

Hauri, E., Wang, J., Dixon, J.E., King, P.L., Mandeville, C., Newman, S., 2002. SIMS analysis of volatiles in silicate glasses 1. Calibration, matrix effects and comparisons with FTIR. Chem. Geol. 183, 99–114.

Hess, K.-U., Dingwell, D.B., 1996. Viscosities of hydrous leucogranitic melts: a non-Arrhenian model. Am. Mineral. 81, 1297–1300.

Holloway, J.R., Dixon, J.E., Pawley, A.R., 1992. An internally heated, rapid-quench, high-pressure vessel. Am. Mineral. 77, 643–646.

Hui, H., Zhang, Y., 2007. Toward a general viscosity equation for natural anhydrous and hydrous silicate melts. Geochim. Cosmochim. Acta 71, 403–416.

Hui, H., Zhang, Y., Xu, Z., Behrens, H., 2008. Pressure dependence of the speciation of dissolved water in rhyolitic melts. Geochim. Cosmochim. Acta 72, 3229–3240.

Humphreys, M.C.S., Menand, T., Blundy, J.D., Klimm, K., 2008. Magma ascent rates in explosive eruptions: constraints from H_2O diffusion in melt inclusions. Earth Planet. Sci. Lett. 270, 25–40.

Iacono Marziano, G., Schmidt, B.C., Dolfi, D., 2007. Equilibrium and disequilibrium degassing of a phonolitic melt (Vesuvius AD 79 “white pumice”) simulated by decompression experiments. J. Volcanol. Geotherm. Res. 161, 151–164.

Lange, R.A., Carmichael, I.S.E., 1987. Densities of Na_2O–K_2O–CaO–MgO–FeO–Fe_2O_3–Al_2O_3–TiO_2–SiO_2 liquids: new measurements and derived partial molar properties. Geochim. Cosmochim. Acta 51, 2931–2946.

Larsen, J.F., 2008. Heterogeneous bubble nucleation and disequilibrium H_2O exsolution in Vesuvius K-phonolite melts. J. Volcanol. Geotherm. Res. 175, 278–288.

Larsen, J.F., Denis, M.-H., Gardner, J.E., 2004. Experimental study of bubble coalescence in rhyolitic and phonolitic melts. Geochim. Cosmochim. Acta 68, 333–344.

Liu, Y., Zhang, Y., Behrens, H., 2005. Solubility of H_2O in rhyolitic melts at low pressures and a new empirical model for mixed H_2O–CO_2 solubility in rhyolitic melts. J. Volcanol. Geotherm. Res. 143, 219–235.

Long, W., Friedman, I., 1968. The refractive index of experimentally hydrated rhyolite glass. Am. Mineral. 53, 1754–1756.

Newbury, D.E., 1975. Image formation in the scanning electron microscope. In: Goldstein, J.I., Yakowitz, H. (Eds.), Practical Scanning Electron Microscopy. Plenum Press, New York, pp. 95–148.

Newman, S., Epstein, S., Stolper, E.M., 1988. Water, carbon dioxide, and hydrogen isotopes in glasses from the ca. 1340 A.D. eruption of the Mono Craters, California: constraints on degassing phenomena and initial volatile content. J. Volcanol. Geotherm. Res. 35, 75–96.

Newman, S., Lowenstern, J.B., 2002. VolatileCalc: a silicate melt–H_2O–CO_2 solution model written in Visual Basic for Excel. Comput. Geosci. 28, 597–604.

Newman, S., Stolper, E.M., Epstein, S., 1986. Measurement of water in rhyolitic glasses: calibration of an infrared spectroscopic technique. Am. Mineral. 71, 1527–1541.

Ni, H., Zhang, Y., 2008. H_2O diffusion models in rhyolitic melt with new high pressure data. Chem. Geol. 250, 68–78.

Nichols, A.R.L., Wysoczanski, R.J., 2007. Using micro-FTIR spectroscopy to measure volatile contents in small and unexposed inclusions hosted in olivine crystals. Chem. Geol. 242, 371–384.

Nowak, M., Behrens, H., 2001. Water in rhyolitic magmas: getting a grip on a slippery problem. Earth Planet. Sci. Lett. 184, 515–522.

Ochs III, F.A., Lange, R.A., 1997. The partial molar volume, thermal expansivity, and compressibility of H_2O in $NaAlSi_3O_8$ liquid: new measurements and an internally consistent model. Contrib. Mineral. Petrol. 129, 155–165.

Silver, L.A., Ihinger, P.D., Stolper, E.M., 1990. The influence of bulk composition on the speciation of water in silicate glasses. Contrib. Mineral. Petrol. 104, 142–162.

Sparks, R.S.J., 1978. The dynamics of bubble formation and growth in magmas: a review and analysis. J. Volcanol. Geotherm. Res. 3, 1–37.

Stolper, E.M., 1982a. The speciation of water in silicate melts. Geochim. Cosmochim. Acta 46, 2609–2620.

Stolper, E.M., 1982b. Water in silicate glasses: an infrared spectroscopic study. Contrib. Mineral. Petrol. 81, 1–17.

Stolper, E.M., 1989. Temperature dependence of the speciation of water in rhyolitic melts and glasses. Am. Mineral. 74, 1247–1257.

Watkins, J.M., Manga, M., DePaolo, D.J., 2012. Bubble geobarometry: a record of pressure changes, degassing, and regassing at Mono Craters, California. Geology 40, 699–702.

Wertheim, D., Gillmore, G., 2014. Application of confocal microscopy for surface and volume imaging of solid state nuclear track detectors. J. Microsc. 254, 42–46.

Xu, Z., Zhang, Y., 2002. Quench rates in air, water, and liquid nitrogen, and inference of temperature in volcanic eruption columns. Earth Planet. Sci. Lett. 200, 315–330.

Zhang, Y., Jenkins, J., Xu, Z., 1997. Kinetics of the reaction $H_2O + O = 2OH$ in rhyolitics glasses upon cooling: geospeedometry and comparison with glass transition. Geochim. Cosmochim. Acta 61, 2167–2173.

Zhang, Y., Stolper, E.M., Ihinger, P.D., 1995. Kinetics of the reaction $H_2O + O = 2OH$ in rhyolitic and albitic glasses: preliminary results. Am. Mineral. 80, 593–612.
Zhang, Y., Stolper, E.M., Wasserburg, G.J., 1991. Diffusion of water in rhyolitic glasses. Geochim. Cosmochim. Acta 55, 441–456.
Zhang, Y., Xu, Z., Behrens, H., 2000. Hydrous species geospeedometer in rhyolite: improved calibration and application. Geochim. Cosmochim. Acta 64, 3347–3355.
Zhang, Y., Xu, Z., Liu, Y., 2003. Viscosity of hydrous rhyolitic melts inferred from kinetic experiments, and a new viscosity model. Am. Mineral. 88, 1741–1752.